ADVANCED MATERIALS INTERFACES

Supporting Information

for *Adv. Mater. Interfaces,* DOI: 10.1002/admi.202201406

Thru-Hole Epitaxy: A Highway for Controllable and Transferable Epitaxial Growth

Dongsoo Jang, Chulwoo Ahn, Youngjun Lee, Seungjun Lee, Hyunkyu Lee, Donghoi Kim, Yongsun Kim, Ji-Yong Park, Young-Kyun Kwon, Jaewu Choi,* and Chinkyo Kim**

Supplementary Information for

Thru-hole Epitaxy: A Highway for Controllable and Transferable Epitaxial Growth

Dongsoo Jang Chulwoo Ahn Youngjun Lee Seungjun Lee Hyunkyu Lee Donghoi Kim Yongsun Kim Ji-Yong Park Young-Kyun Kwon Jaewu Choi* Chinkyo Kim**

D. Jang, Y. Lee, S. Lee, Y.-K. Kwon, C. Kim
Department of Physics, Kyung Hee University, Seoul 02447, Korea
Email Address: ykkwon@khu.ac.kr, ckim@khu.ac.kr
C. Ahn, H. Lee, D. Kim, Y.-K. Kwon, J. Choi, C. Kim
Department of Information Display, Kyung Hee University, Seoul 02447, Korea
Email Address: ykkwon@khu.ac.kr, jaewuchoi@khu.ac.kr, ckim@khu.ac.kr
Y. Kim and J.-Y. Park
Department of Physics and Energy Systems Research, Ajou University, Suwon 16499, Korea

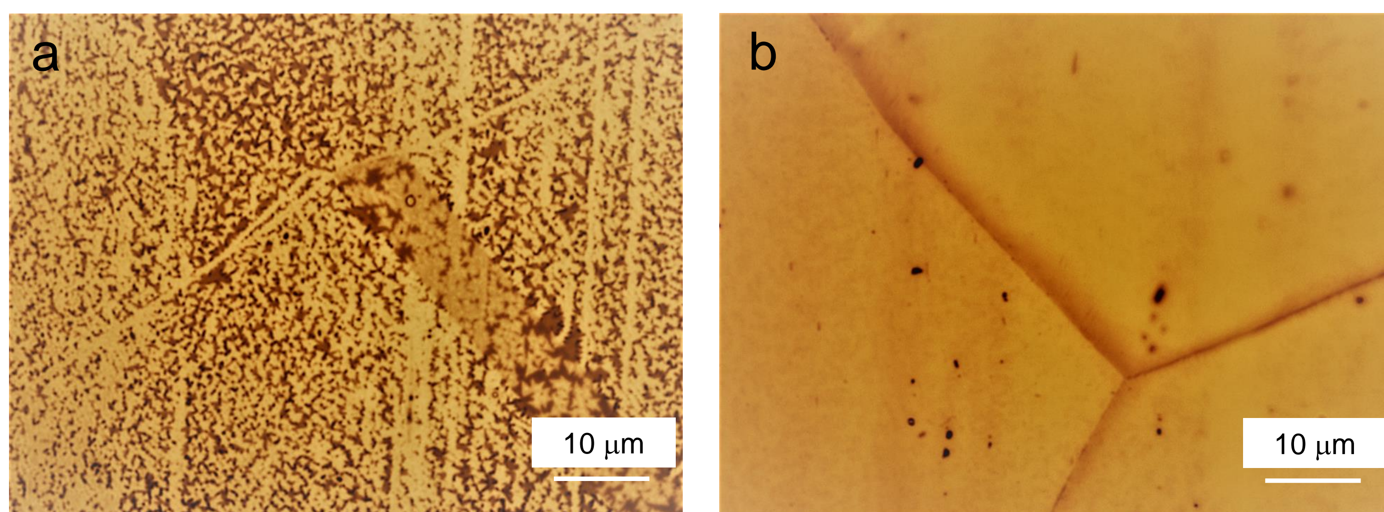

Figure S1: Polycrystalline *h*-BN grown on a Cu foil. Optical microscopy image of (a) 10-min- and (b) 2-hr-grown *h*-BN on a polycrystalline Cu foil after 1-min-oxidation at 200°C for a clear distinction between h-BN covered area and exposed Cu foil. The 10-min-grown *h*-BN domains with a typical triangular shape were misaligned with one another, implying that *h*-BN was polycrystalline. On the other hand, the 2-hr-grown h-BN fully covered a Cu foil as shown in (b). Note that the color correction was made for clarity.

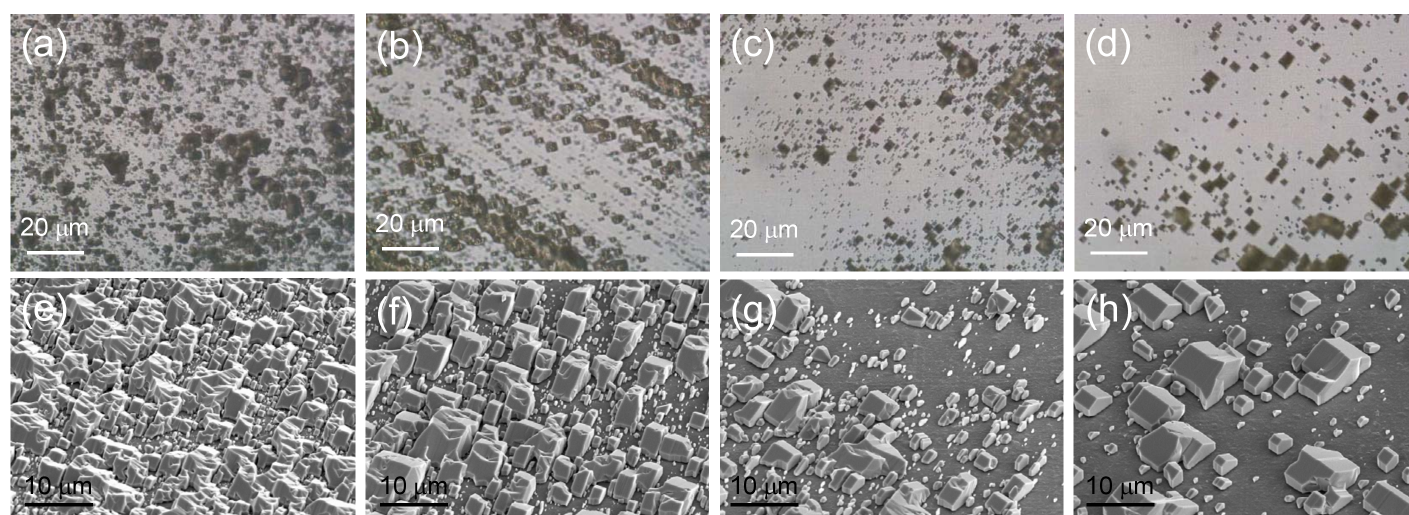

Figure S2: Decreased density of GaN domains with the increased thickness of a *h*-BN space layer. (a–d) Optical microscopy images of and (e–h) SEIs of $[11\bar{2}0]$-oriented GaN domains grown over *h*-BN transferred onto *r*-sapphire substrates once, four, six, and eight times to adjust the thickness of a *h*-BN space layer. Those GaN domains are aligned in parallel with one another. It is clear that the density of GaN domains decreased with the increased number of transfer times of *h*-BN.

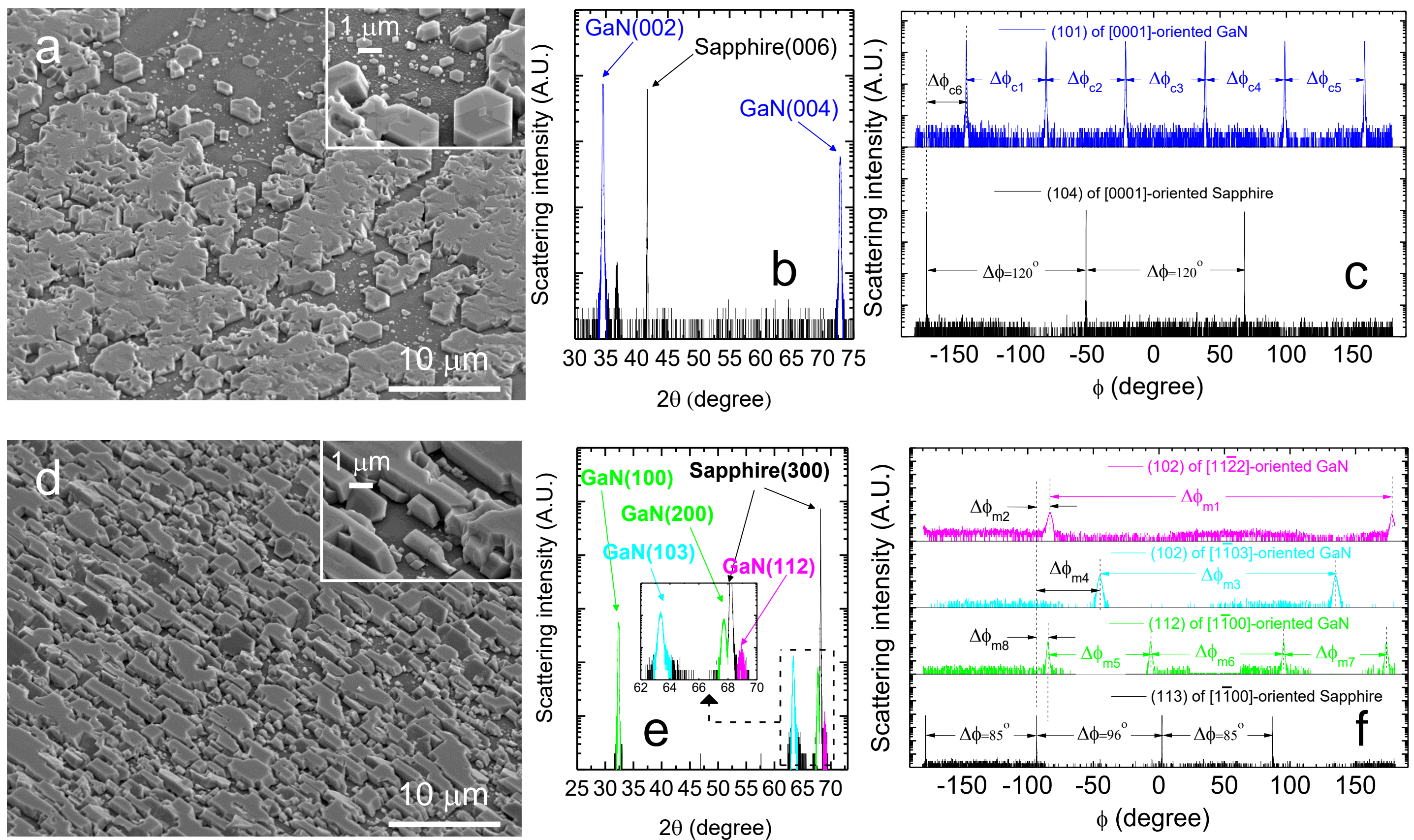

Figure S3: **Crystallographically aligned GaN domains grown on *h*-BN/*c*-sapphire and *h*-BN/*m*-sapphire. (a) Secondary electron image (SEI) and (b, c) XRD data of GaN domains grown on *h*-BN transferred once onto *c*-sapphire as well as (d–f) on *h*-BN/*m*-sapphire. Note that there is a (101) Bragg peak of GaN near $2\theta = 37^{\circ}$ the intensity of which is several orders smaller than that of the *c*-GaN (002) Bragg peak.**

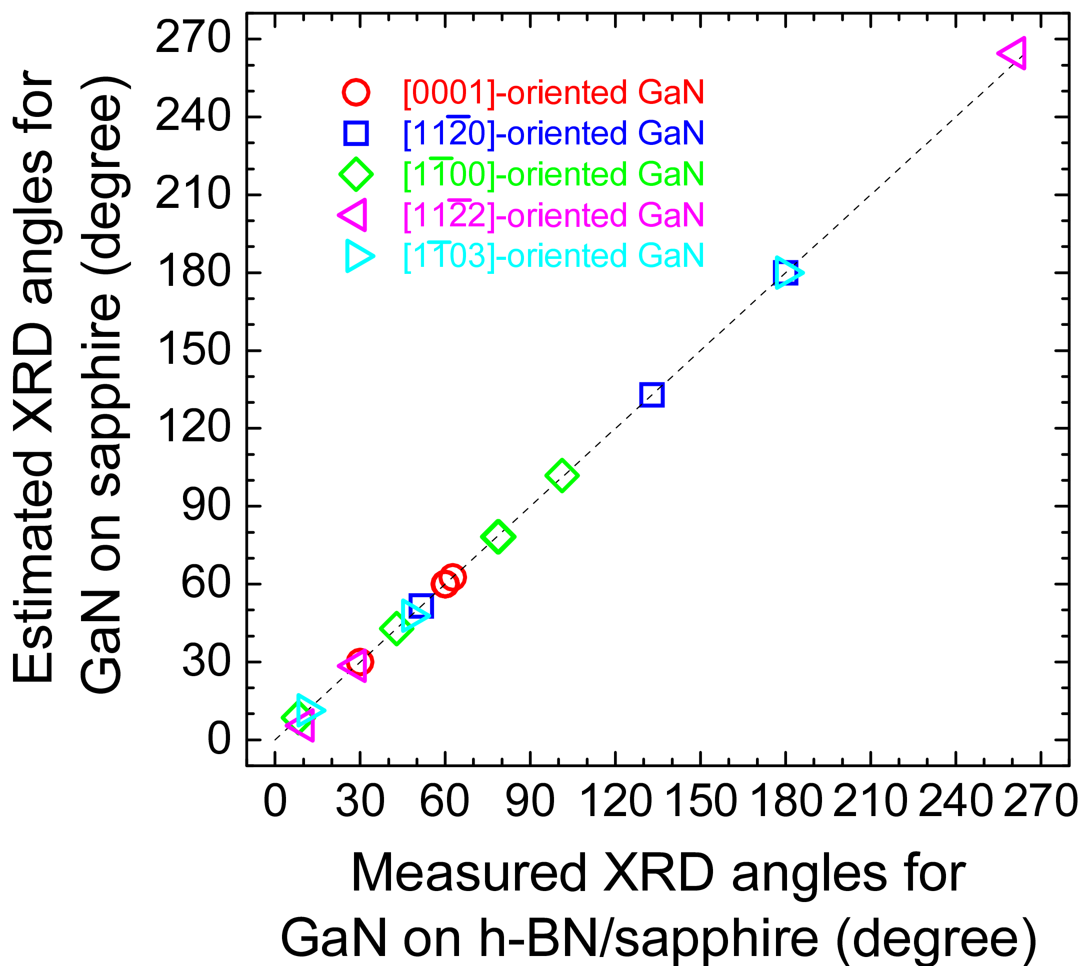

Figure S4: Consistency between crystallographic alignments of GaN domains grown on *h*-BN/sapphire and bare sapphire. Experimentally measured XRD angles for GaN domains grown over *h*-BN on *r*-, *c*-, and *m*-sapphire substrates shown in Fig. 1 in the main text and Fig. S3 vs. the estimated XRD angles for GaN grown on their corresponding bare sapphire substrates. This consistency verifies the crystallographic alignment of GaN with the underlying sapphire substrates in spite of a *h*-BN space layer.

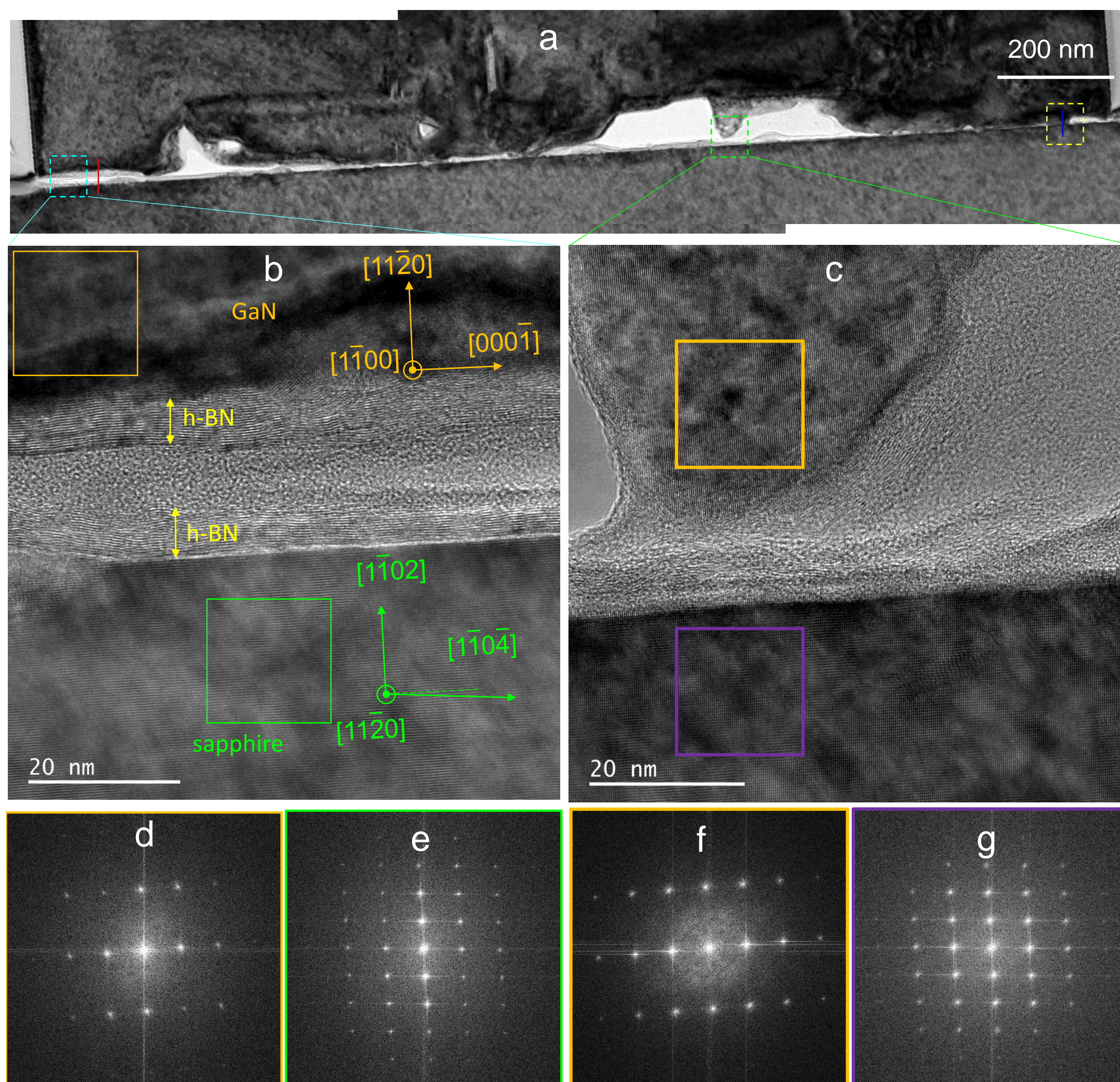

Figure S5: **Seemingly beyond RE based on TEM images at first sight. (a) Magnified stitched images of the interface region enclosed by the red dashed box shown in Fig. S6b. (b–c) High-resolution cross-sectional TEM image, taken from the region enclosed by cyan and green dashed boxes shown in (a). (d–e) The fast Fourier transforms (FFTs) of [11$\bar{2}$0]-oriented GaN and *r*-sapphire enclosed respectively by the orange and green boxes marked in (b). (f–g) The fast Fourier transforms (FFTs) of the GaN and the *r*-sapphire regions enclosed respectively by the orange and violet boxes in (c). Note that there are crystalline *h*-BN layers, marked in (b), which embed carbon-based amorphous materials. (Fig. S7a) They are thought to originate from the residue of PMMA used for *h*-BN transfer and do not make any influence on this growth process. The slight tilt of a line along the laterally aligned Bragg peaks of [11$\bar{2}$0]-oriented GaN with respect to that of *r*-sapphire shown in FFT is due to the characteristics of crystallographic orientation of *r*-sapphire, not due to the stress relaxation. The yellow dashed box in (a) marks the region whose high-resolution TEM image is shown in Fig. 2(a).**

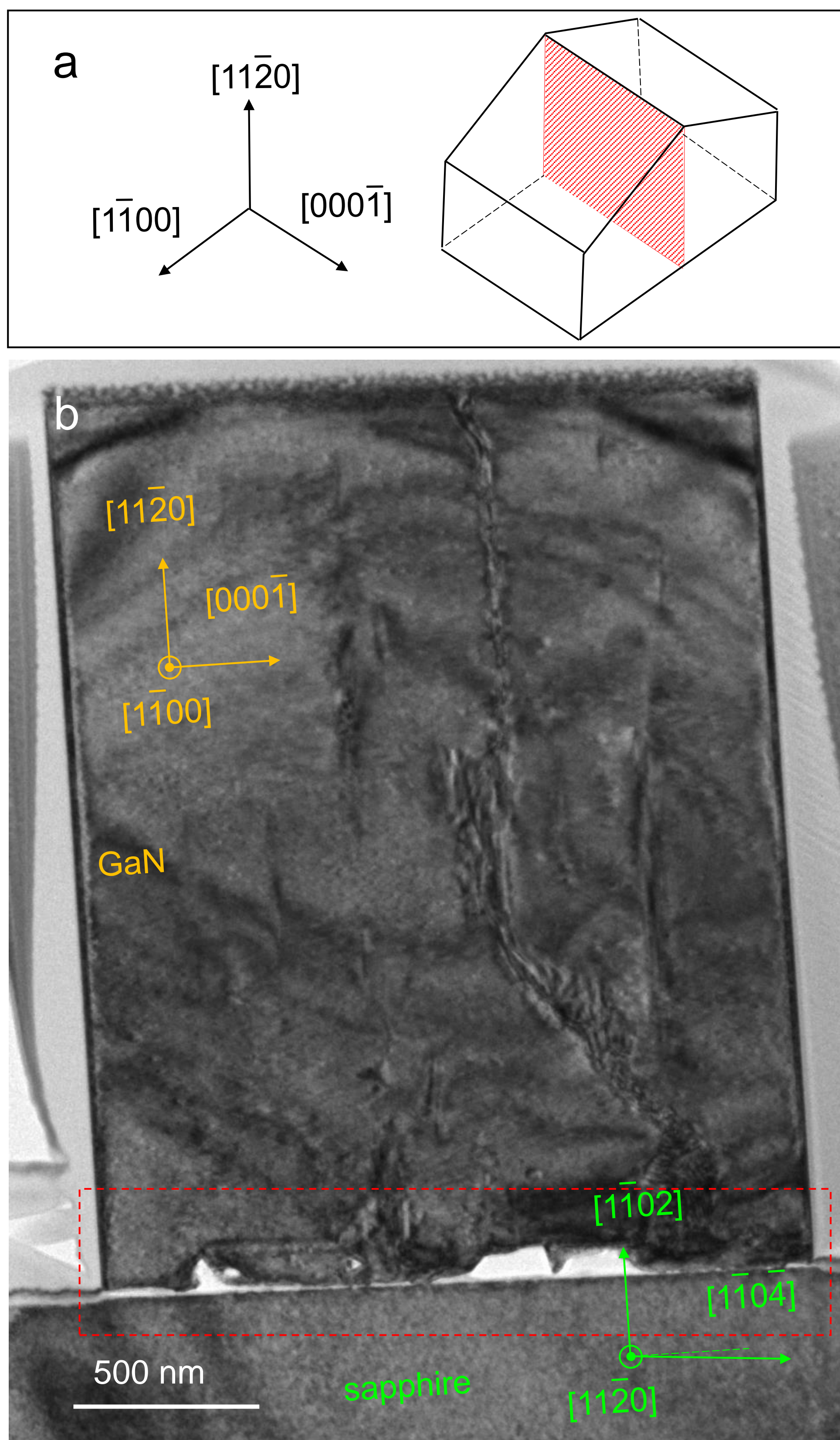

Figure S6: Schematic diagram for cross-sectioning and overview of a cross-sectional TEM image. (a) Schematic diagram of a gable-roof-shaped GaN domain cross-sectioned for TEM measurement. (b) Cross-sectional TEM image of a single domain of GaN grown on h-BN transferred eight times onto r-sapphire.

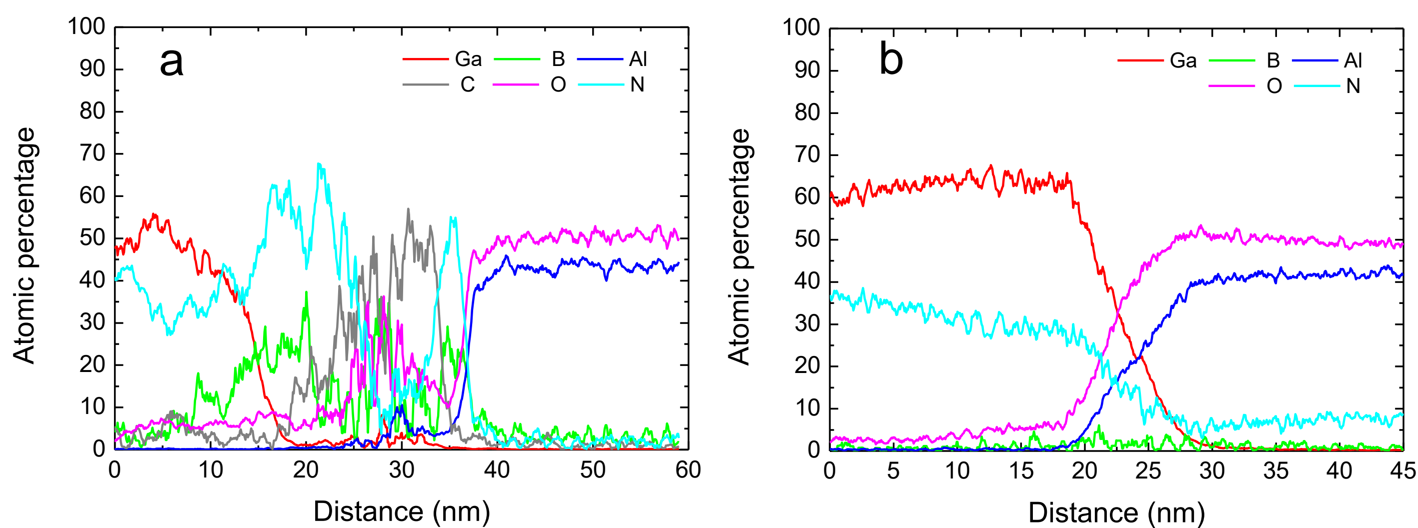

Figure S7: Chemical analysis across the interface. (a) Energy-dispersive X-ray spectroscopy (EDS) line scan, taken along the red line near the cyan dashed box where GaN and sapphire were separated by space layer material as shown in Fig. S5a and Fig. S5b in the main text. The existence of *h*-BN across the interface was chemically confirmed. The amorphous material between the h-BN layers shown in Fig. S5b turns out to be carbon-based. (b) EDS line scan taken along the blue line within the yellow dashed box where the connectedness was established as shown in Fig. S5a and Fig. 2a in the main text. There is no sign of *h*-BN across the interface indicating the connectedness.

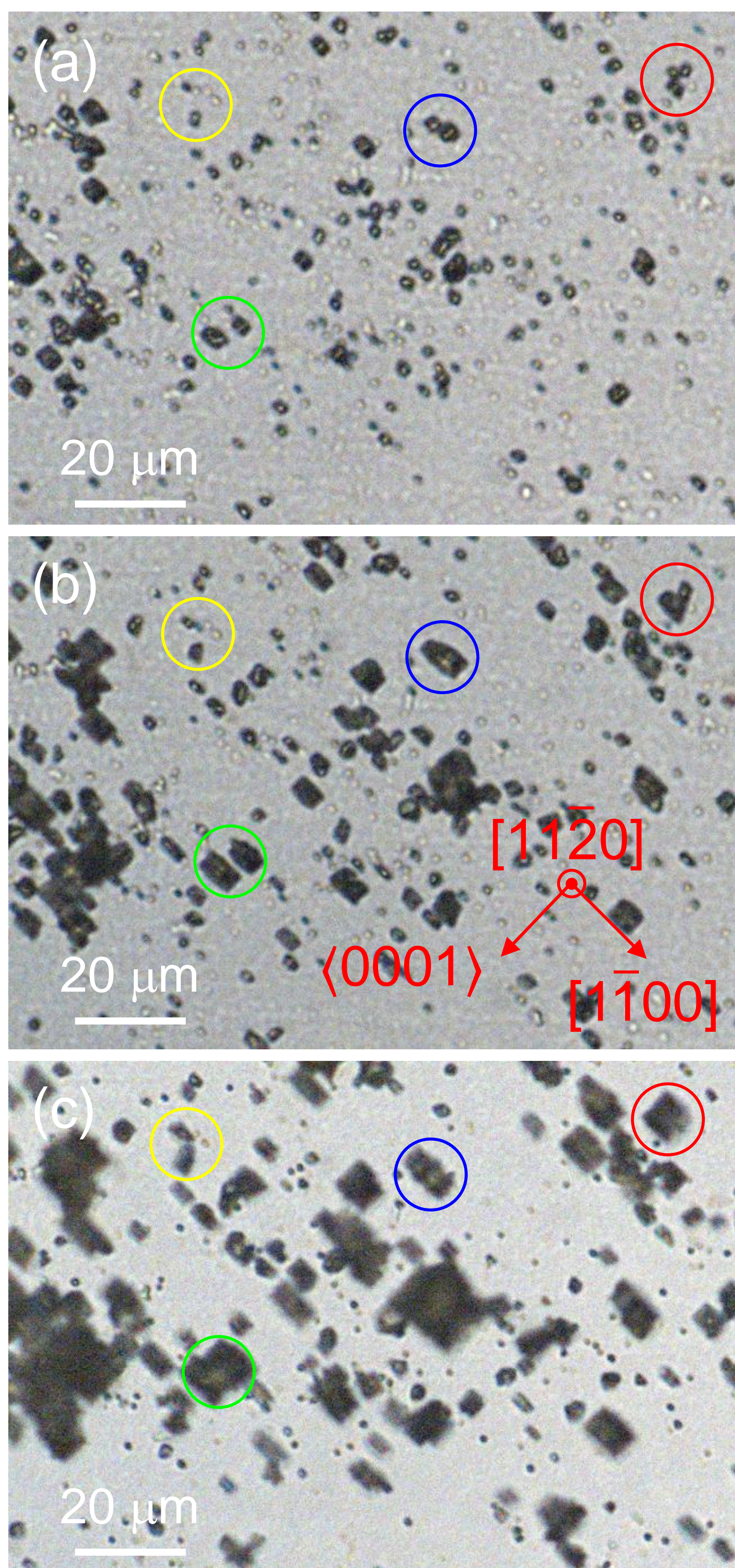

Figure S8: Effect of thru-holes on nucleation. Optical microscopy images of GaN domains grown for (a) 9 minutes, (b) 13 minutes, and (c) 19 minutes. The colored circles reveal the lateral/vertical growth and coalescence of individual domains with increased growth time. Note that there were no additionally nucleated domains with increased growth time.

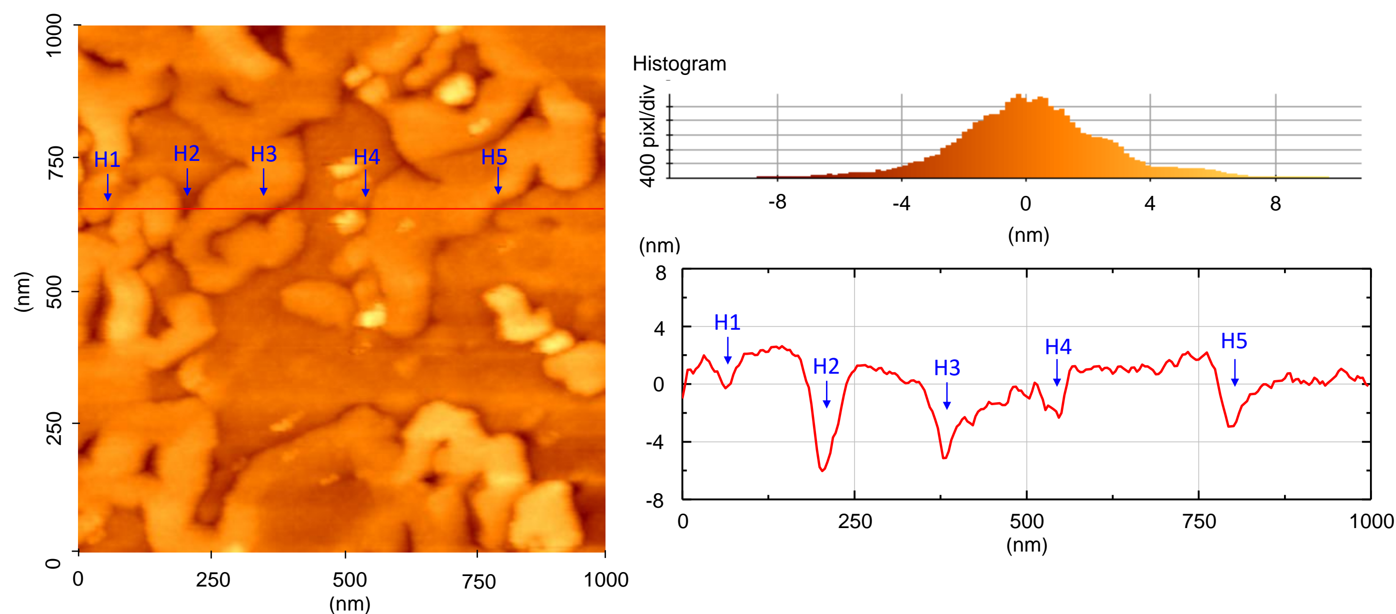

Figure S9: AFM topography image of h-BN transferred onto r-sapphire showing holes and connected holes. The topography clearly reveals that the holes (represented as dark regions in this image) are not isolated but connected just like the argument given for the survival of thru-holes. The height profile along the red line is shown on the right. This line profile also reveals that some holes are deeper than others because only some of the holes exposed to the top surface can be thru-holes.

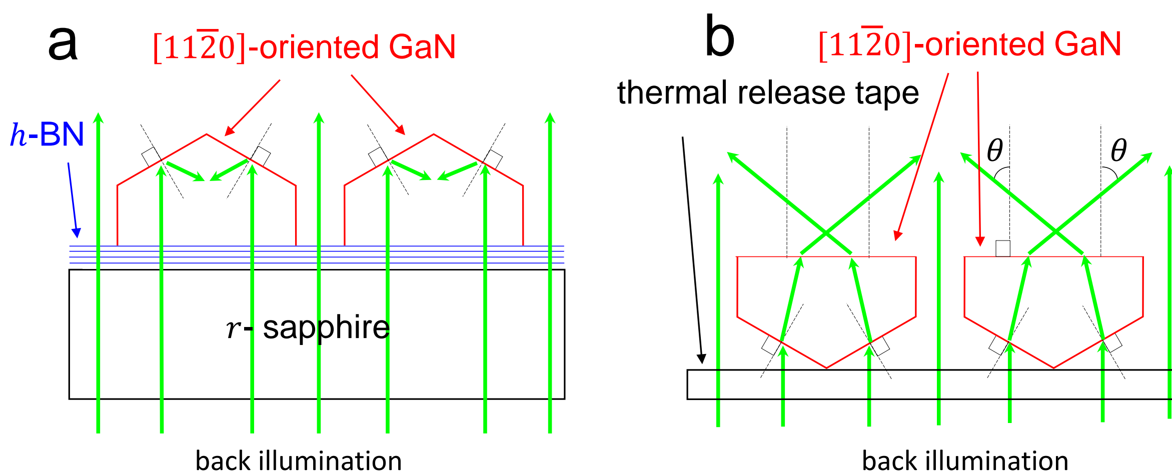

Figure S10: The reason why the [11$\bar{2}$0]-oriented GaN domains with gable-roof shape look dark. Ray-tracing diagrams for (a) as-grown and (b) detached GaN domains corresponding to the images shown in Fig. 3a and c. The incident light in (**a**) is totally internally reflected with an incidence angle of 30°, which is larger than the critical angle of GaN in a full visible range. On the other hand, the incident light in (**b**) exits GaN after refraction twice with a final exit angle larger than the maximum acceptance angle in a full visible range determined by an objective lens. These are two reasons why [11$\bar{2}$0]-oriented GaN domains with the gable-roof shape in Fig. 3 are dark and the other regions look bright in the back illumination configuration.

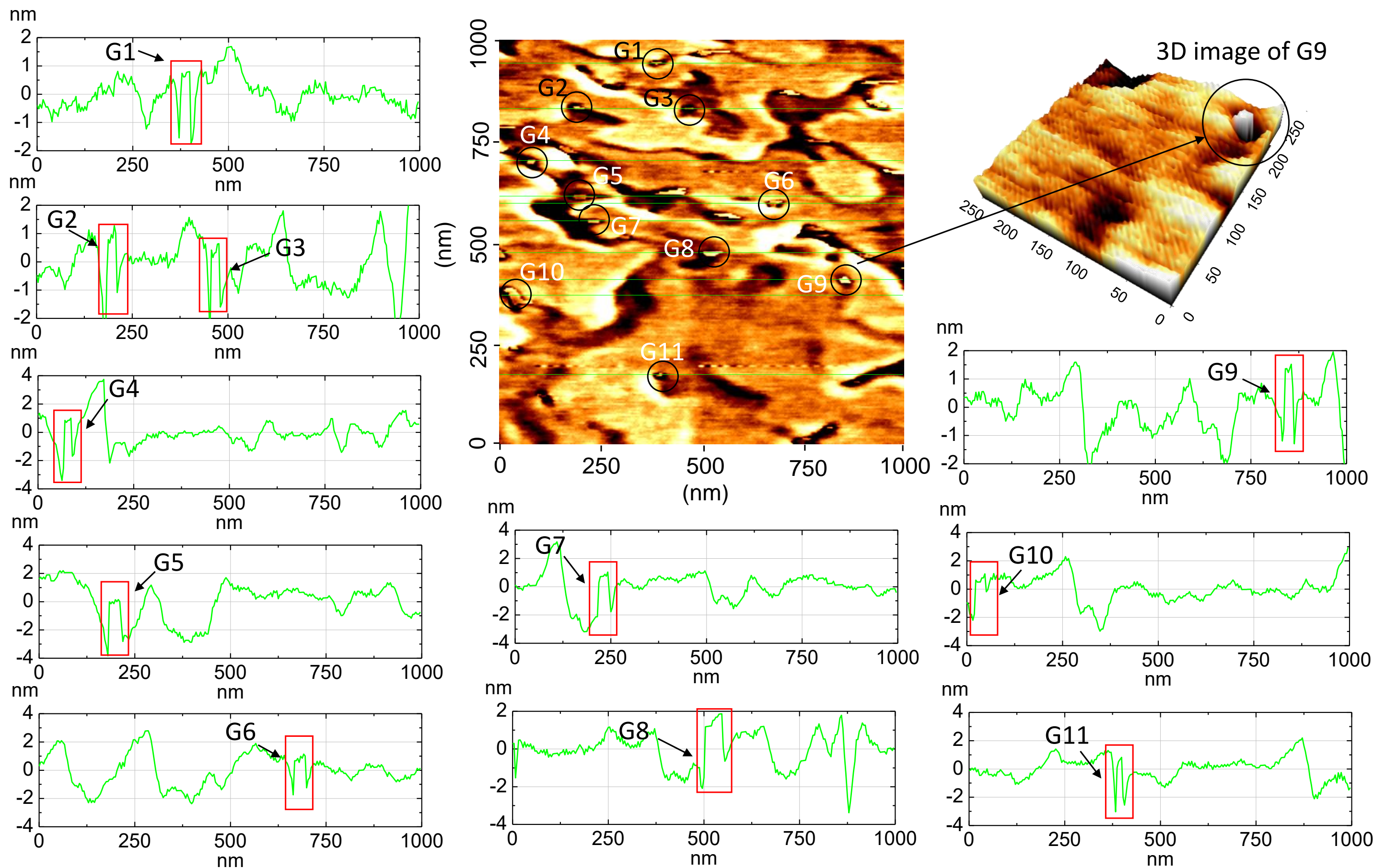

Figure S11: AFM topography of GaN stumps within thru-holes of h-BN. AFM topography image of h-BN on c-sapphire after GaN was detached by thermal release tape. As clearly seen, the bright regions surrounded by dark regions (marked by circles with G-Arabic-number indexed) represent GaN stumps nucleated on sapphire through thru-holes. Line profiles through each GaN stump are also displayed. 3D image of G9 also clearly shows that the GaN stump was within a thru-hole. This topography and line profiles through GaN stumps once again reveal a few important features of this thru-hole epitaxy: (1) GaN was nucleated on sapphire through thru-holes, (2) the width of GaN stumps nucleated on sapphire was consistently small enough to allow detachment of GaN to be readily accomplishable, which suggests that the weakest parts in this sample are where there is GaN within thru-holes due to its small width. From the area of GaN domains left on the substrate after exfoliation of GaN as shown in Fig.S11, the areal density of thru-holes can be roughly estimated if the area of GaN domains left is approximately comparable to the area of thru-hole. From the eleven holes in size of about 40nm×40nm in Fig. S11, the areal density can be roughly estimated to be 1.76×10^{-2} apart from the estimation error associated with a non-uniform spatial distribution of thru-holes. It should be noted that this estimated areal density simply corresponds to that of nominal thru-holes, not that of laterally connected thru-holes, which are truly responsible for thru-hole epitaxy, as described in the main manuscript. Of course, the areal density of GaN nucleation sites is supposed to be equal to that of thru-holes in this estimation.

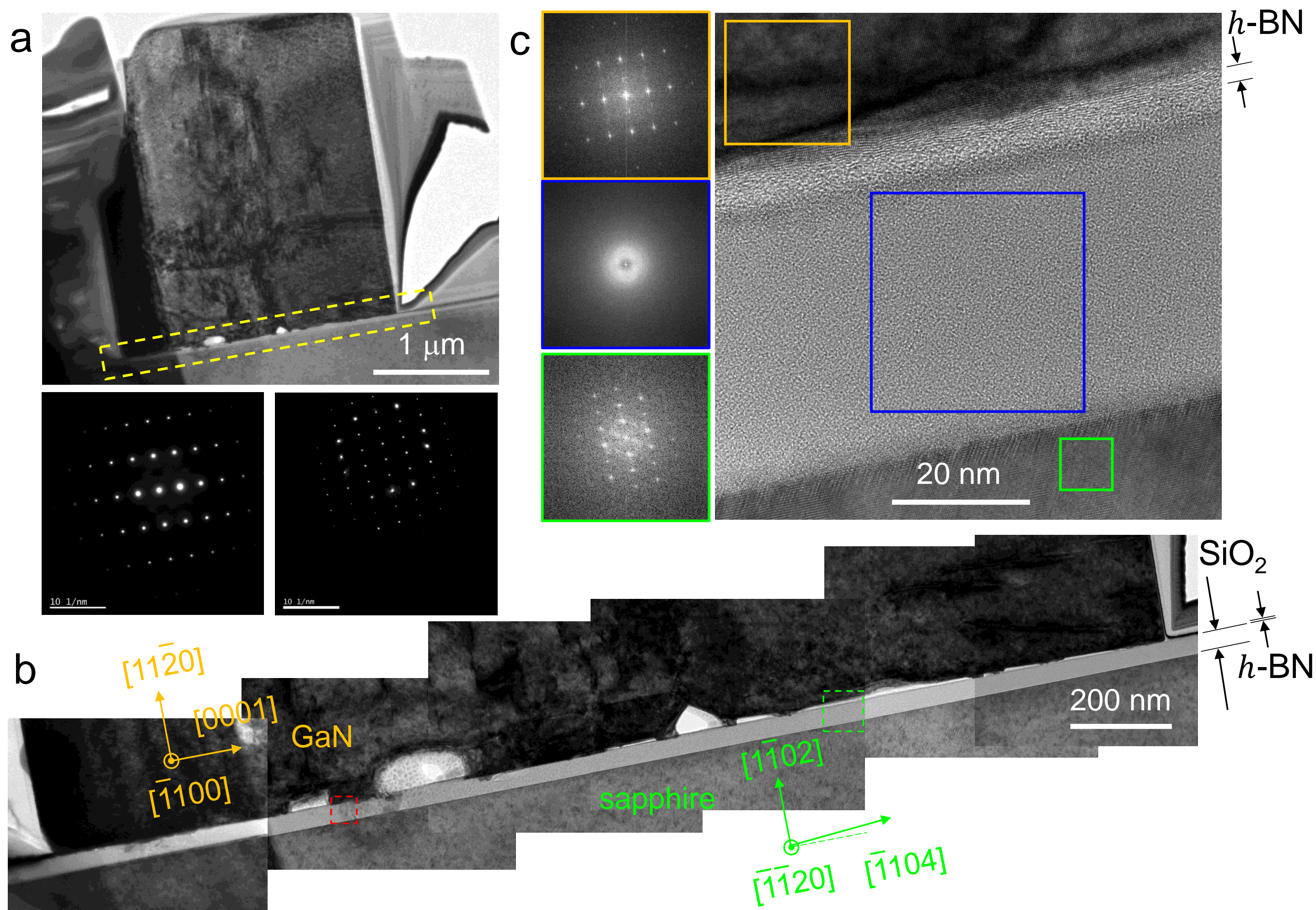

Figure S12: **TEM images across the interface of GaN/h-BN/SiO_2/r-sapphire. (a) Cross-sectional TEM image of a single domain of GaN grown on h-BN/SiO_2/r-sapphire with selected area diffraction patterns of GaN (left) and sapphire (right). (b) Magnified stitched images of the interface region enclosed by the yellow dashed box shown in (a). (c) Magnified TEM image of the region enclosed by the green dashed box shown in (b) and the FFTs of the GaN, SiO_2, and the r-sapphire regions enclosed respectively by the orange, blue, and green boxes. It is clear that there is a h-BN space layer on top of the SiO_2 film. The high-resolution TEM image, taken from the region with a thru-hole enclosed by the red dashed box, is shown in Fig. 4d in the main text. The FFTs reveal that [11$\bar{2}$0]-oriented GaN is aligned with r-sapphire, suggesting the lateral overgrowth initiated by the thru-hole epitaxy. Note that the FFT of the SiO_2 region shows no crystallinity at all.**

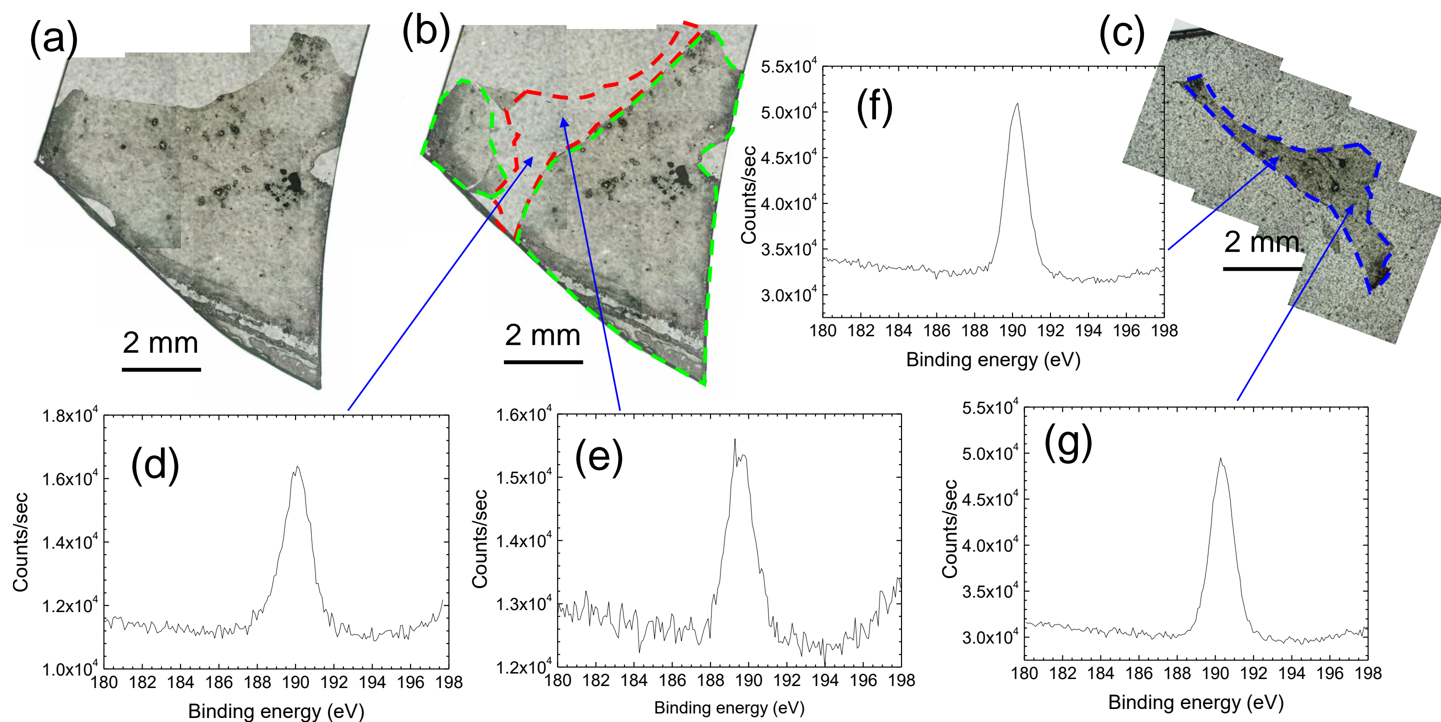

Figure S13: Detachability near the critical connectedness. Stitched optical microscopy images of (a) as-grown GaN domains on a one-time transferred h-BN space layer on a c-sapphire substrate, (b) the c-sapphire substrate after the GaN domains were detached by using a handy thermal release tape, and (c) the detached GaN domains on the thermal release tape. The regions enclosed by the red and blue dashed lines represent the exposed c-sapphire and detached GaN. The region enclosed by the green dashed line represents the undetached GaN. In this case, the connectedness is too much, resulting in partial detachment of GaN. The extent of the connectedness can be easily reduced by increasing the number of transfer times as shown in Fig. S2, so that the detachability efficiency is much improved. XPS spectra from the front side of sapphire after GaN was detached by a TRT ((d) and (e)) and from the backside of detached GaN ((f) and (g)). XPS spectra show that B 1s peak ($\sim$190.2 eV) was observed on both the backside of detached GaN and the front side of the sapphire substrate, indicating that h-BN existed both on detached GaN and sapphire.

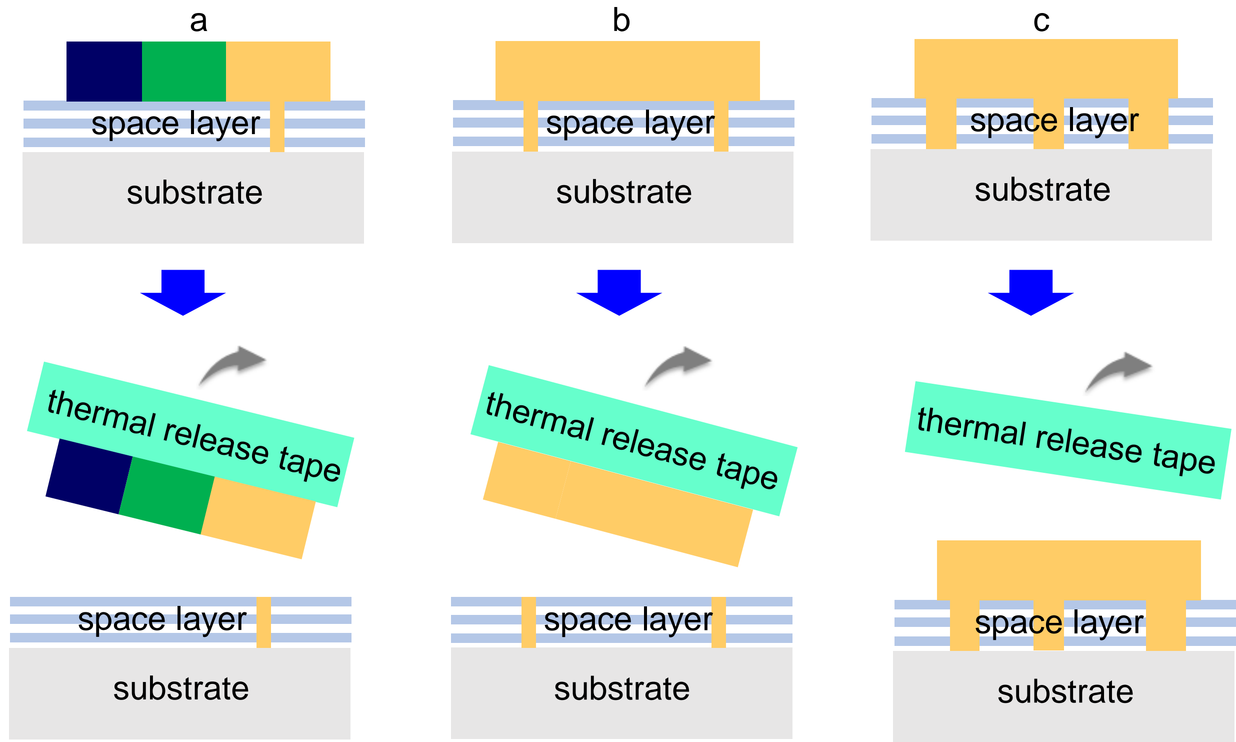

size & density	$L < L_c^{\mathrm{CA}}$ or $\sigma < \sigma_c^{\mathrm{CA}}$	$L_c^{\mathrm{CA}} < L < L_c^{\mathrm{FD}}$ and $\sigma_c^{\mathrm{CA}} < \sigma < \sigma_c^{\mathrm{FD}}$	$L_c^{\mathrm{FD}} < L$ or $\sigma_c^{\mathrm{FD}} < \sigma$
CA / FD	X / O	O / O	O / X

Figure S14: Optimal regime of THE. Schematic diagrams and a table show the conditions for the optimal regime of THE. Domains marked in orange represent well-aligned ones while those in navy blue and green represent misaligned ones.

S1 Misinterpretation in the previous computational results for RE

There are several papers reporting vdWE on *h*-BN or graphene/graphite. Nevertheless, it is very challenging to achieve such vdWE or to grow 3D single-crystalline films on dangling-bond-free 2D materials,[1] because of small potential fluctuation and the absence of nucleation centers. To overcome this limitation in most cases, various defects playing roles as nucleation centers were introduced on a 2D surface using surface modification techniques.[2, 3] Moreover, vdWE has been observed relatively more often on *h*-BN than on graphene because the potential fluctuation on the latter surface is even smaller than that on the former surface. Another important point is whether the potential profile reflects the symmetry of underlying substrate or 2D material for remote or vdwE, respectively, or not. As clearly shown in our manuscript, the teleported potential fluctuation does not reflect the symmetry of the underlying substrate, whereas the surface potential profile of *h*-BN or graphene does show its complete symmetry. Also, the formation of a large nucleate with a radius larger than the critical radius is an important key issue for epitaxy, and our estimated potential fluctuation across the surface of 2D material/substrate is even larger than that of vdwE. However, we would like to point out two points: (i) the structural configurations of large nucleates formed during the growth process would be quasi-random and thus their symmetry would not be necessarily consistent with the symmetry of substrate; and (ii) even if there is a large nucleate that has the same symmetry of substrate by accident, it is unlikely that such nucleate settles on 2D material with crystallographic alignment to the underlying substrate, because the potential profile of 2D material/substrate does not reflect the symmetry of the underlying substrate as mentioned above and in our manuscript.

Some of the previous papers on remote epitaxy showed that their potential/charge profiles reflect the characteristics of the underlying substrates. It turned out that such results had been obtained only under certain constrained conditions as described in the following. In the paper by Kong *et al.*[4], which is one of the original papers explaining the concept of remote epitaxy, they did not show the *total* potential distribution U_{tot} of 2D material/substrate, which is the true potential governing growth processes. Instead, they intentionally calculated a potential distribution defined as $U = U_{\mathrm{tot}} - U_{\mathrm{2D}}$, to reflect mainly substrate contribution by subtracting the 2D material contribution, U_{2D}. We would like to emphasize again that the true potential governing growth processes is not this potential difference, but the total potential. Moreover, they used small supercell sizes to enforce commensurability between 2D material and substrate by introducing large strain, resulting in the creation of an artificial symmetry reflecting that of the underlying substrate. Such structural constraint is, of course, unavoidable since a periodic system is required in calculations. That is why we considered various stacking configurations (relatively different orientations and supercell sizes) of 2D material/substrate to exclude constraint-induced artifacts in our calculation. As shown in Fig. 6 in our main manuscript and Fig. 8, U_{tot} depends strongly on the stacking configuration (relative orientation and supercell size) and thus does not follow the symmetry of the underlying substrate. Another work[5] showed the charge density with a small supercell instead of potential distribution. In that paper, they computed charge density using $\rho = \rho_{\mathrm{tot}} - \rho_{\mathrm{2D}}$ to extract the substrate contribution, rather than the total charge density ρ_{tot} of 2D material/substrate, which is a true charge density responsible for the growth process. Therefore, the existence of vdwE cannot be direct evidence for remote epitaxy, the concept of which is still not regarded to be validated by DFT calculations, but rather strongly questionable.

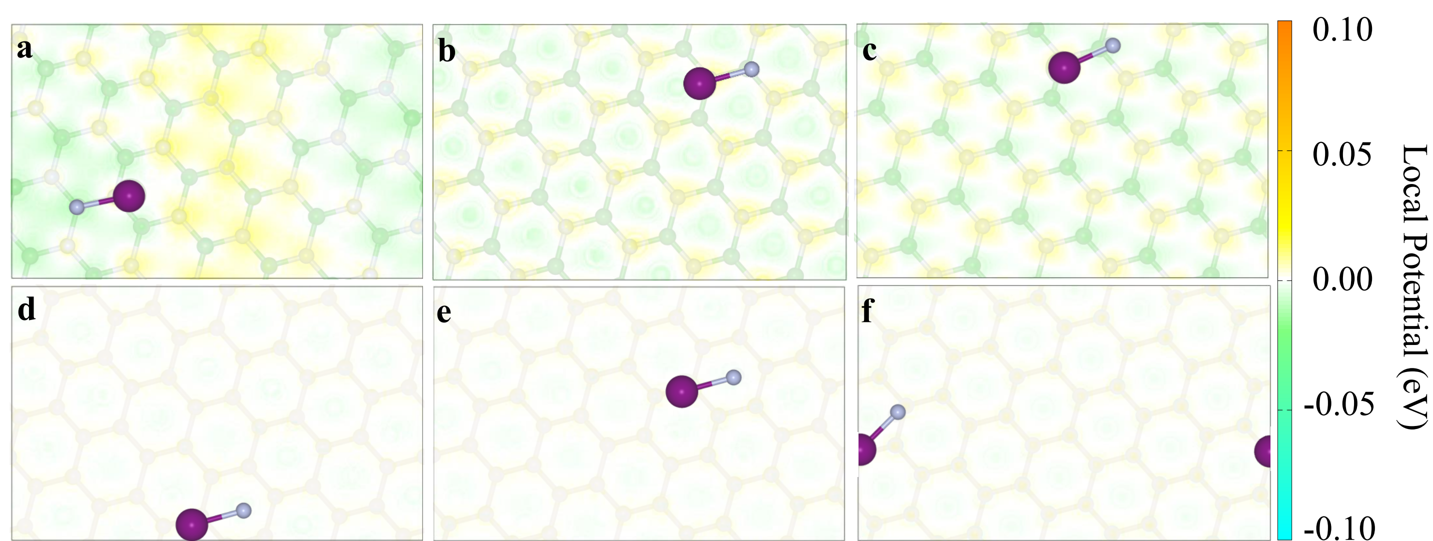

Figure S15: Surface potential profiles over graphene and h-BN multilayers on r-sapphire. Surface potential profiles evaluated at $d = 3.0$ Å from the respective top surfaces for (a) bi-, (b) tri-, and (c) hex-layers of h-BN, and (d) bi-, (e) tri-, and (f) hex-layers of graphene, all of which are on r-sapphire. ΔV shown in Fig. 6**e** in the main text was evaluated where the Ga-N dimer is placed. The topmost atomic layer overlaid on each color-coded potential profile is a guide for the eyes. The color bar shows the potential variation relative to the average potential value set to be zero. Note that the indistinguishable color variation in (d–f) indicates that the potential variations on graphene overlayers are negligibly small.

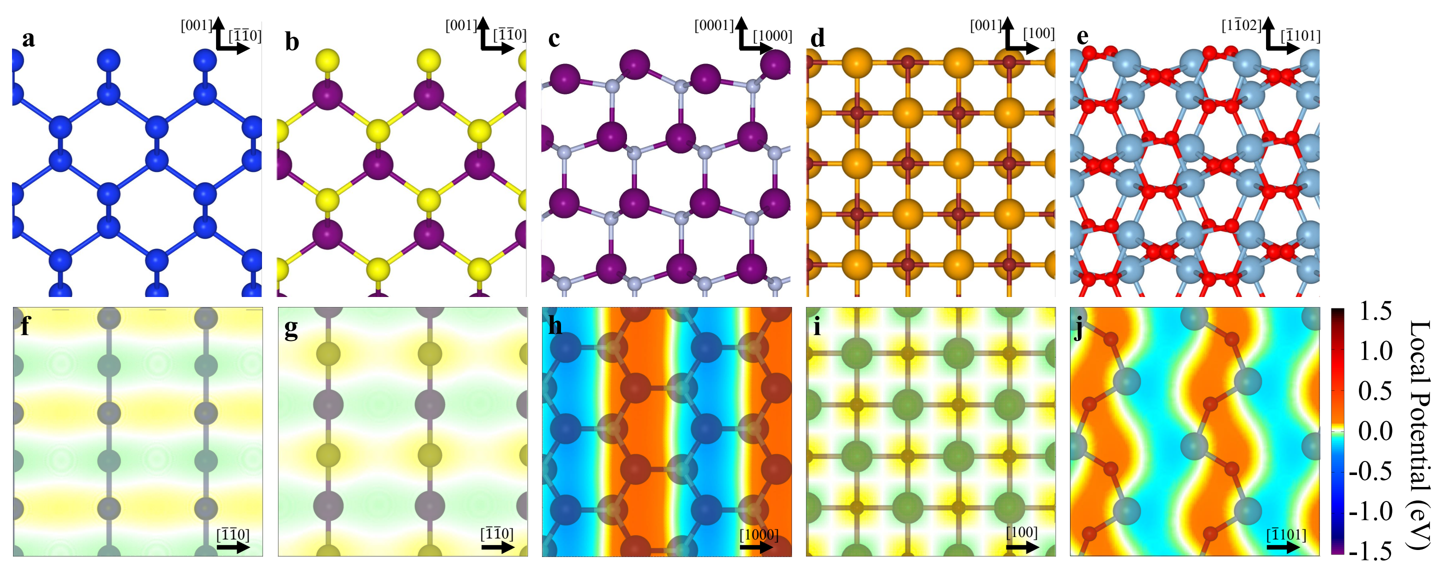

Figure S16: Surface potential profiles over various substrates. Side views of (a) Si, (b) GaAs, (c) GaN, (d) LiF, and (e) r-sapphire. (f–j) The color-coded surface potential variations calculated at 3.0 Å above the corresponding top surface. The topmost atomic layer overlaid on each color-coded potential profile is guide for the eyes. The color bar shows the potential variation relative to the average potential value set to be zero. Blue, purple, yellow, grey, ocher, brown, red, and skyblue spheres indicate Si, Ga, As, N, Li, F, O, and Al atoms, respectively.

S2 Artifacts caused by the choice of supercells

The potential orientations do not appear to change with the relative rotation in Fig. 8, but in fact it does in case of 19.1° rotation as shown in Fig. 8 (i). In addition, as can be clearly seen, the side of a black parallelogram has a different length from that of a red parallelogram for each case of different stacking configurations, indicating that the periodicity changes with the relative rotation. Even in these cases, the supercells were created by enforcing artificial commensurability between *h*-BN and *c*-sapphire. For more realistic and practical situations, there would be no artificial commensurability, so that the change of potential orientation and periodicity with the relative rotation between *h*-BN and r-sapphire would be more dramatic. The fact that the potential of the combined system of 2D material/substrate does not follow the orientation and periodicity of the underlying substrate becomes more vivid in cases where 2D material has a symmetry different from that of the substrate, for example, *h*-BN on *r*-sapphire or *m*-sapphire as shown in Fig. 6 in the main manuscript and in Fig. S15 and Fig. S16. Therefore, the potential fluctuation of 2D material/substrate does not truly reflect the orientation and periodicity of the underlying substrate if the artifact originating from artificial stacking configurations is simply excluded.

S3 The features of RE from the viewpoint of THE

Crystallographic alignment of a grown film with an underlying substrate:

The crystallographic alignment with the underlying substrate established without direct bonding in RE is really fascinating, but the crystallographic alignment is a natural consequence of epitaxial growth involving direct bonding between a film and an underlying substrate. So, this evidence can be readily understood in terms of THE as well.

Crystallographic alignment limited by layer number of 2D space material:

The crystallographic alignment in RE was observed only on monolayer or bilayer graphene. Such alignment in this limited condition was regarded as the main feature of reported RE. This can be also easily and self-consistently explained by THE as follows. If there are holes in 2D layers, the stacking of 2D layers containing holes would decrease the number density of thru-holes, so that the number density of potential nucleation spots would decrease. One important factor here is that how fast the number density of thru-holes decreases with an increasing number of stacking. If the quality of the 2D layer is excellent, only a few stacking would immediately block all the holes whereas thru-holes still survive even after stacking several times if it is mediocre. In any case, if the number density and size of thru-holes get smaller than critical values, THE becomes less dominant over growth with misaligned orientation (GwMO). (See Figure S14(a))

Ionicity dependence of crystallographic alignment:

In reported RE, ionicity was regarded as a key factor to obtain crystallographic alignment. Such aligned domains of ionic material can be readily explained by THE as long as the size and number density of thru-holes are larger than their critical values for crystallographic alignment. These critical values vary with materials properties such as ionicity. For example, if two different materials with and without ionicity are separately grown on the same 2D insertion layer on the substrate made of their respective materials, adatoms of the nonionic material would be less attracted toward thru-holes by the exposed substrate than those of the ionic material. That is because the range of attractive interaction from the ***exposed area*** of the nonionic material is much shorter than that of the ionic material. Thus, the formation of misaligned domains on the 2D space layer would be more probable with the nonionic material than the ionic material because the actual size and number density of thru-holes are smaller than critical values for the nonionic material but larger than those for the ionic material. In other words, nonionic material would be more likely to be grown as GwMO than ionic material on the same 2D space layer. It should be noted that this kind of ionicity-dependence of interaction range is not typically observed in conventional ELOG because the size of an individual hole or opening area is so sufficiently large that stochastic diffusion of adatoms toward opening areas is more dominant.

Easy detachability:

It should be noted that easy detachability does not necessarily suggest a complete absence of direct bonding between a film and an underlying substrate. Instead, it simply indicates that the adhesive force between the grown film and a thermal release tape is large enough to break the binding force between the grown film and a space layer/substrate. It can be easily inferred that increasing the layer number of 2D space material would decrease the number density of thru-holes, so that detachability would be improved as well. Moreover, the detachability would be enhanced by reducing the size of thru-holes. In both situations, however, GwMO begins to coexist with THE. On the other hand, as the size and number den-

sity of thru-holes become(s) larger the detachment of a grown film or even a single domain by a thermal release tape would become less possible and eventually impossible with the crystallographic alignment enhanced, indicating that ELOG becomes dominant.

References

[1] D. Liang, T. Wei, J. Wang, J. Li, *Nano Energy* **2020**, *69* 104463.

[2] Y. Feng, X. Yang, Z. Zhang, D. Kang, J. Zhang, K. Liu, X. Li, J. Shen, F. Liu, T. Wang, P. Ji, F. Xu, N. Tang, T. Yu, X. Wang, D. Yu, W. Ge, B. Shen, *Advanced Functional Materials* **2019**, *29*, 42 1905056.

[3] M. De Luca, X. Cartoixà, J. Martín-Sánchez, M. López-Suárez, R. Trotta, R. Rurali, I. Zardo, *2D Materials* **2020**, *7*, 2 025004.

[4] W. Kong, H. Li, K. Qiao, Y. Kim, K. Lee, Y. Nie, D. Lee, T. Osadchy, R. J. Molnar, D. K. Gaskill, et al., *Nature Mater.* **2018**, *17*, 11 999.

[5] J. Jeong, Q. Wang, J. Cha, D. K. Jin, D. H. Shin, S. Kwon, B. K. Kang, J. H. Jang, W. S. Yang, Y. S. Choi, et al., *Science Advances* **2020**, *6*, 23 eaaz5180.